Seismic evidence for widespread deep crustal deformation caused by extension in the western US

M.P. Moschetti[1,2†], M.H. Ritzwoller[1],
F.-C. Lin[1] and Y. Yang[1]

1 - Center for Imaging the Earth's Interior,
Department of Physics, University of Colorado at Boulder,
Campus Box 390, Boulder, CO 80309, USA,

2 - (curently at) Geologic Hazards Science Center,
U.S. Geological Survey,
Denver, CO 80225, USA
† To whom correspondence should be directed: mmoschetti@usgs.gov

February 12, 2010

1

Laboratory experiments have established that many earth materials are strongly anisotropic[1]. Observations of azimuthal[2,3] and radial[4,5] anisotropy in the upper mantle are attributed to the lattice-preferred orientation (LPO) of olivine caused by the shear strains associated with deformation, and provide some of the most direct evidence for deformation and flow within Earth's interior. Although observations of crustal radial anisotropy would improve understanding of crustal deformation and flow patterns resulting from tectonic processes, large-scale observations have been limited only to regions of particularly thick crust[6]. Here we show that new observations from ambient noise tomography in the western US reveal strong radial anisotropy in the deep (middle to lower) crust confined primarily to the geological provinces that have undergone significant extension during the Cenozoic Era (since $\sim$65 Ma)[7,8]. The coincidence of crustal radial anisotropy with the extensional provinces of the western US suggests that the radial anisotropy results from the LPO of anisotropic crustal minerals

caused by extensional deformation. Conversely, the observation of crustal radial anisotropy across the extensional provinces in the western US provides new support for the hypothesis that the deep crust within these regions has undergone widespread and relatively uniform strain in response to crustal thinning and extension[9,10,11].

To infer information about crustal anisotropy in the western US from surface wave dispersion requires measurements at periods below 20 s, but waves at these periods are strongly scattered and attenuated as they propagate from distant earthquakes. Because surface waves with periods greater than 20 s are primarily sensitive to wavespeed structures below about 25 km depth, only regions with very thick crust have been amenable to surface wave inversions for crustal anisotropy[6]. The inference of the 3-D distribution of anisotropy in regions with normal to thin continental crust is now possible, however, using surface wave dispersion measurements at periods from 6 to 20 s recovered from ambient seismic noise[12,13]. The dispersion data from ambient noise tomography (ANT) have been combined with longer period ($>$ 40 s) Rayleigh wave phase speed measurements from multiple plane wave earthquake tomography (MPWT) to generate high resolution images of isotropic S-wave speeds in the crust and uppermost mantle across the western US[14]. We show similarly high resolution images of the radial anisotropy of the crust and uppermost mantle in the western US and discuss implications for deformation within the deep crust.

We follow the ambient noise data processing protocol of Bensen et al.[15] to obtain cross-correlations between long timeseries (up to several years) of ambient noise recorded at pairs of seismic stations from the USArray Transportable Array (TA). The cross-correlations provide three-component, inter-station "empirical Green's functions" on which Rayleigh and Love wave group and phase speed measurements are obtained at periods from 6 to 40 s[16,17]. These measurements are strongly sensitive to S-wave speeds in the crust and uppermost mantle and facilitate the imaging of structures shallower than those typically resolved using teleseismic earthquake observations alone[18]. At each point in time, the TA comprises about 400 broadband stations on a 70 km grid (Figure 1a). We processed waveforms from 526 TA stations acquired between October 2004 and December 2007 to obtain Rayleigh and Love wave dispersion measurements along more than 120,000 inter-station paths (Supplementary Figure 1). Love wave group speed measurements are less reliable than the other measurements, and we retain only measurements of Rayleigh wave group (RG) and phase speeds (RP) and Love wave phase speeds (LP) in the following bands: RG, 6 – 40 s; RP, 6 – 40 s; LP, 8 – 32 s. Inversion of the dispersion measurements initiates with

the construction of dispersion maps. The maps based on dispersion measurements from ambient noise (e.g., Figures 1b–d) are constructed using a traditional straight ray tomographic method[19]. Measurement of Rayleigh wave phase speeds by MPWT is described by Yang et al.[14], but the maps have been updated to extend the study area and to incorporate data from additional earthquakes. The combined period band of the Rayleigh wave phase speed measurements extends from 6 to100 s.

We report results of inversions for radial anisotropy (transverse isotropy with a radial symmetry axis) in the crust and uppermost mantle underlying the western US. Radial anisotropy, also referred to as polarization anisotropy, manifests itself as the difference in the speeds of horizontally- and vertically-polarized S-waves (V_{SH} and V_{SV}, respectively). It is inferred by simultaneously interpreting the dispersion characteristics of Rayleigh and Love waves, which depend predominantly on V_{SV} and V_{SH}, respectively. In particular, it is inferred from the "Rayleigh-Love discrepancy", which is a measure of the misfit to the Rayleigh and Love wave dispersion curves that results from a best fitting isotropic model ($V_S = V_{SH} = V_{SV}$).

To illustrate the existence and nature of the Rayleigh-Love discrepancy in the western US and to localize its source, we present three inversions. Inversion I defines a purely isotropic reference state in which there is a single S-wave speed at each depth in the crust and upper mantle. Inversion II is a perturbation to the isotropic reference model in which radial anisotropy is permitted in the upper mantle but not in the crust. Inversion III further perturbs the model by allowing radial anisotropy in the crust with an additional perturbation in the upper mantle. In each case, the data are the same: local dispersion curves with uncertainties (see Methods) that are constructed from the dispersion maps on a 0.5°-by-0.5° grid across the study region (e.g., Figure 2a for a point in central Nevada). Forward modeling is performed with the radially anisotropic code MINEOS[20] and the model space is sampled with a Monte Carlo method[21].

An example best-fitting model for a point in central Nevada produced in Inversion I is shown in Figure 2b. Because data at periods greater than 30 s are generally well fit by the V_S models of Inversions I, II and III, we present reduced chi-squared misfit, hereafter "chi-squared", in the 6 to 30 s period band. The range of acceptable models for this point and how those models fit the dispersion data are shown in Supplementary Figures 3a and b. The isotropic models from Inversion I produce a large Rayleigh-Love discrepancy across most of the western US, as seen in Figure 2c. The spatially-averaged chi-squared misfit from the best fitting model of Inversion I is $\chi^2_I = 12.2$. At locations with large chi-squared values (e.g., central Nevada, Figure 2a,

$\chi^2 = 29.2$), Love wave phase speeds computed from the isotropic model under-predict the observed speeds above about 15 s period, whereas the Rayleigh wave phase and group speeds are slightly over-predicted between 20 and 30 s period and severely over-predicted below 20 s. Because more Rayleigh than Love wave measurements are inverted, the isotropic model tends to fit the Rayleigh wave data better than the Love wave data.

Inversion II attempts to resolve this Rayleigh-Love discrepancy by introducing radial anisotropy in the upper mantle as a single depth-independent perturbation between V_{SH} and V_{SV}. We permit radial anisotropy with an amplitude ($2\,|V_{SH} - V_{SV}|\,/(V_{SH} + V_{SV})$) of up to 10%, consistent with the largest values observed by Nettles and Dziewonski[22]. The introduction of mantle anisotropy (e.g., Figure 2e) improves data fit significantly (Figure 2d and f, $\chi^2 = 10.5$) compared with the isotropic model, reducing overall misfit to $\chi^2_{II} = 5.7$, a 77% variance reduction. Regions of relatively poor data fit persist, however. Residual misfit to the Rayleigh wave phase and group speeds is largest at periods less than about 15 and 20 s period, respectively, whereas misfit to the Love wave phase speeds remains largest between about 15 and 25 s period (e.g., Figure 2d). The amplitude of radial anisotropy in the mantle that results from this inversion is shown in Supplementary Figure 4.

Significant further reduction in the Rayleigh-Love discrepancy requires the introduction of radial anisotropy in the crust. The inability of other physically reasonable model parameters to resolve the discrepancy is demonstrated in Supplementary Information. In Inversion III, we perturb the best fitting model from Inversion II by allowing a constant anisotropic perturbation to middle and lower crustal S-wave speeds and an additional perturbation to mantle anisotropy. This inversion exhibits a trade-off between the amplitudes of radial anisotropy in the crust and mantle, with the resulting amplitude of crustal and mantle anisotropy negatively correlating across all tectonic regions, reflected as a negative slope of the misfit ellipses shown in Figure 3. In some regions (e.g., Sierra Nevada, much of the Colorado Plateau; Figures 3b and c) radial anisotropy is not required in either the crust or mantle to fit the data and in other regions (e.g., Columbia Plateau, Oregon; Figure 3a) it is required in either the crust or mantle. But, in extensional provinces within the western US (e.g., Basin and Range, Rocky Mountain Basin and Range, and the Omineca extended belt), positive crustal anisotropy ($V_{SH} > V_{SV}$) (Figures 3d–f) is required irrespective of the strength of mantle anisotropy. Although the amplitude of crustal anisotropy in these regions depends on the amplitude of the mantle anisotropy, the sign of the crustal radial anisotropy is unique and positive.

We refer to the regions with clear positive crustal radial anisotropy as the "anisotropic crustal regions". Outside of the anisotropic crustal regions, crustal anisotropy is generally not required by the data.

To construct a single model in Inversion III, we constrain upper mantle anisotropy to lie within 2% of the best-fitting model from Inversion II (Supplementary Figure 4). Because of the negative correlation between crustal and mantle anisotropy, this constraint produces a conservative (lower bound) estimate of the amplitude of crustal anisotropy. Example results for central Nevada are shown in Figures 4a and b ($\chi^2 = 3.2$). The mean amplitudes of radial anisotropy in the crust and mantle across the anisotropic crustal regions are 3.6% and 5.3%, respectively. Only positive radial anisotropy is observed. Misfit resulting from Inversion III is presented in Figure 4c, and mean chi-squared across the study region is $\chi^2_{III} = 2.8$, a 95% variance reduction compared to the isotropic model from Inversion I. The introduction of crustal radial anisotropy resolves the residual Rayleigh-Love discrepancy to $\chi^2 < 4$, on average, except in discrete areas outside the primary anisotropic crustal regions where other structural variables may need to be introduced to improve data fit further (e.g., Olympic Peninsula, Great Valley of California, Salton Trough, parts of the High Lava Plains of Oregon, southern Cascades, Yellowstone). Residual misfit is discussed further by Moschetti et al.[23].

The amplitude of radial anisotropy in the crust and mantle of the best fitting model from Inversion III is shown in Figures 4d and e, respectively. The resulting patterns of strong crustal radial anisotropy correlate with the predominant extensional provinces in the region. Cenozoic extension in the western US is believed to have been primarily confined to the Basin and Range (BR), the Rocky Mountains Basin and Range (RMBR), and the Omineca extended belt (OEB) provinces[7] (see Figure 1a). Average extension across these provinces has been estimated to range up to 100%[7,8]. Strong crustal radial anisotropy is evident across nearly the entire BR province and terminates abruptly near its edges; e.g., along the Wasatch and Sierra Nevada Ranges, along the Snake River Plain, and along the Colorado Plateau. Crustal anisotropic amplitudes greater than 5% are present in all three extensional provinces. The largest continuous region of strong amplitude radial anisotropy (>4%) occurs in central Nevada. Observations of seismic anisotropy in the mantle are routinely ascribed to the LPO of mantle minerals and are used to infer characteristics about the mantle flow field[24,25]. Because of the relative dearth of observations of middle to lower crustal anisotropy, such inferences are not common for the crust.

Various studies, however, suggest widespread lower crustal deformation

in response to extension in the western US[9,10,11]. Heretofore, regional-scale observations of crustal seismic anisotropy have not existed to support or overturn this hypothesis. We interpret the observed crustal radial anisotropy to result from the LPO of seismically anisotropic crustal minerals induced by the finite strains accompanying extension. The shear strains associated with crustal extension preferentially orient the seismic slow axes along the vertical axis[26]. At middle to lower crustal depths, micro-fractures are closed by lithostatic stresses[27] and the LPO of micas and amphiboles would significantly contribute to seismic anisotropy[1,26,28]. Improved vertical resolution of radial anisotropy is needed to estimate the contributions from specific minerals in this region. Our results suggest, however, that the deep crustal response to extension in the western US is widespread and relatively uniform.

2 Methods summary

For a radially anisotropic medium, the elasticity tensor reduces to a symmetric matrix with twelve non-zero elements and five independent components. These five components may be represented by the Love parameters – A, C, F, L, and N[29]. Horizontally propagating seismic wave speeds are given by $V_P = (A/\rho)^{\frac{1}{2}}$, $V_{SH} = (N/\rho)^{\frac{1}{2}}$, and $V_{SV} = (L/\rho)^{\frac{1}{2}}$, where ρ is density. The non-dimensional parameters, $\xi = N/L = (V_{SH}/V_{SV})^2$, $\phi = C/A = (V_{PH}/V_{PV})^2$, and $\eta = F/(A - 2L)$, are commonly introduced, where, for an isotropic medium, all parameters equal one. Because surface wave dispersion measurements are less sensitive to ϕ and η than to ξ, we perturb only ξ from its isotropic value. We find that perturbations to the ϕ and η parameters do not significantly affect our conclusions (see Supplementary Information).

Rayleigh and Love wave dispersion curves are simultaneously inverted using the radially anisotropic code MINEOS[20] to calculate surface wave dispersion curves and the Neighbourhood Algorithm[21] for model space sampling. We invert for layer thicknesses, V_P/V_S, V_{SH} and V_{SV} in the crust and for V_{SH} and V_{SV} in the mantle. Uniform model parameterizations and constraints are applied at all grid points. Models are parameterized with four crustal layers (one sedimentary and three underlying crystalline layers) and five cubic B-splines in the mantle. We impose a layer thickness ratio of 1:2:2 for the crystalline crustal layers. Independent perturbations to the sediment and crystalline layer thicknesses are allowed, but total crustal thickness is constrained by receiver function estimates and uncertainties[30].

Crustal S-wave velocities increase monotonically with depth. V_P/V_S, V_{SH} and V_{SV} values are constrained within physically-reasonable bounds which are summarized in Supplementary Table 1.

3 References and Notes

1. Siegesmund, S., Takeshita, T., Kern, H. Anisotropy of V_P and V_S in an amphibolite of the deeper crust and its relationship to the mineralogical, microstructural and textural characteristics of the rock. *Tectonophys.* **157**, 25–38 (1989).

2. Montagner, J.-P., Tanimoto, T. Global upper mantle tomography of seismic velocities and anisotropies. *J. Geophys. Res.* **96**, 20,337–20,351 (1991).

3. Silver, P. G. Seismic anisotropy beneath the continents: Probing the depths of geology. *Ann. Rev. Earth Planet. Sci.* **24**, 385–421 (1996).

4. Ekström, G., Dziewonski, A. M.. The unique anisotropy of the Pacific upper mantle. *Nature* **394**, 168–172 (1998).

5. Shapiro, N. M., Ritzwoller, M. H. Monte-Carlo inversion for a global shear-velocity model of the crust and upper mantle. *Geophys. J. Int.* **151**, 88–105 (2002).

6. Shapiro, N. M., Ritzwoller, M. H., Molnar, P. H., Levin, V. Thinning and flow of Tibetan crust constrained by seismic anisotropy. *Science* **305**, 233–236 (2004).

7. Wernicke, B., in *The Cordilleran Orogen: Conterminous US*, (ed.s B. C. Burchfiel, P. W. Lipman, M. L. Zoback) 553–581 (Geol. Soc. Amer., Boulder, CO, 1992).

8. Janecke, S. U., Translation and breakup of supradetachment basins: Lessons from Grasshopper, Horse Prairie, Medicine Lodge, Muddy Creek and Nicholia Creek Basins, SW Montana. *Geol. Soc. Amer., Abstracts with Programs* **36**, 5 (2004).

9. Block, L., Royden, L. H. Core complex geometries and regional scale flow in the lower crust. *Tectonics* **9**, 557–567 (1990).

10. Bird, P. Lateral extrusion of the lower crust from under high topography, in the isostatic limit. *J. Geophys. Res.* **96**, 10,275–10,286 (1991).

11. Kruse, S., McNutt, M., Phipps-Morgan, J., Royden, L., Wernicke, B. Lithospheric extension near Lake Mead, Nevada - A model for ductile flow in the lower crust. *J. Geophys. Res.* **96**, 4,435–4,456 (1991).

12. Sabra, K. G., Gerstoft, P., Roux, P., Kuperman, W. A., Fehler, M. C. Surface wave tomography from microseisms in Southern California. *Geophys. Res. Lett.* **32**, L14311 (2005).

13. Shapiro, N. M., Campillo, M., Stehly, L., Ritzwoller, M. H. High-resolution surface-wave tomography from ambient seismic noise. *Science* **307**, 1,615–1,618 (2005).

14. Yang, Y., Ritzwoller, M. H., Lin, F.-C., Moschetti, M. P., Shapiro, N. M., The structure of the crust and uppermost mantle beneath the western US revealed by ambient noise and earthquake tomography, *J. Geophys. Res.* **113**, B12310 (2008).

15. Bensen, G. D. et al. Processing seismic ambient noise data to obtain reliable broad-band surface wave dispersion measurements. *Geophys. J. Int.* **169**, 1,239–1,260 (2007).

16. Moschetti, M. P., Ritzwoller, M. H., Shapiro, N. M. Surface wave tomography of the western United States from ambient seismic noise: Rayleigh wave group velocity maps. *Geochem. Geophys. Geosys.* **8**, Q08010 (2007).

17. Lin, F., Moschetti, M. P., Ritzwoller, M. H., Surface wave tomography of the western United States from ambient seismic noise: Rayleigh and Love wave phase velocity maps. *Geophys. J. Int.* **173**, 281–298 (2008).

18. Yang, Y., Ritzwoller, M. H. Teleseismic surface wave tomography in the western US using the Transportable Array component of USArray. *Geophys. Res. Lett.* **5**, L04308 (2008).

19. Barmin, M. P., Ritzwoller, M. H., Levshin, A. L. A fast and reliable method for surface wave tomography. *Pure Appl. Geophys.*, **158**, 1,351–1,375 (2001).

20. Masters, G., Barmin, M. P., Kientz, S. Mineos user manual. *California Institute of Technology* (2007).

21. Sambridge, M. Geophysical inversion with a neighbourhood algorithm – I. Searching a parameter space. *Geophys. J. Int.* **138**, 479–494 (1999).

22. Nettles, M., Dziewonski, A. M. Radially anisotropic shear velocity structure of the upper mantle globally and beneath North America. *J. Geophys. Res.* **113**, B02303 (2008).

23. Moschetti, M. P., Ritzwoller, M. H., Lin, F., Yang, Y. Crustal shear velocity structure of the western US inferred from ambient seismic noise and earthquake data. *submitted, J. Geophys. Res.* (2010).

24. Silver, P. G., Holt, W. E. The mantle flow field beneath western North America. *Science*, **295**, 1,054–1,057 (2002).

25. Becker, T. W., Schulte-Pelkum, V., Blackman, D. K., Kelloff, J. B., O'Connell, R. J. Mantle flow under the western United States from shear wave splitting. *Earth Plan. Sci. Lett.* **247**, 235–251 (2006).

26. Mainprice, D., Nicolas, A. Development of shape and lattice preferred orientations: application to the seismic anisotropy of the lower crust. *J. Struct. Geol.* **11**, 175–189 (1989).

27. Rasolofosaon, P. N. J., Rabbel, W., Siegesmund, S., Vollbrecht, A. Characterization of crack distribution: fabric analysis versus ultrasonic inversion. *Geophys. J. Int.* **141**, 413–424 (2000).

28. Weiss, T., Siegesmund, S., Rabbel, W., Bohlen, T., Pohl, M.. Seismic velocities and anisotropy of the lower continental crust: A review. *Pure Appl. Geophys.* **156**, 97–122 (1999).

29. Love, A. E. H.. *A Treatise on the Theory of Elasticity*, 4th Ed. (Cambridge Univ., 1927).

30. Gilbert, H. J., Fouch, M. J. Complex upper mantle seismic structure across the southern Colorado Plateau/Basin and Range II: Results from receiver function analysis. *Eos Trans. AGU* **88**, S41B-0558 (2007).

4 Acknowledgments

This manuscript benefited from discussions with Kevin Mahan, Craig Jones, and Peter Molnar. Research was supported by NSF-EAR. M.P.M. received

support from an NDSEG Fellowship from the American Society for Engineering Education. The facilities of the IRIS Data Management System, and specifically the IRIS Data Management Center, were used to access the waveform and metadata required in this study.

5 Author contributions

M.P.M. carried out ANT for the Rayleigh wave measurements, performed the 3-D inversion of surface wave dispersion measurements and co-wrote the paper. M.H.R. guided the study design and co-wrote the paper. F.-C. Lin carried out ANT for the Love wave measurements. Y. Yang carried out the MPWT. All authors discussed the results and provided comments on the manuscript.

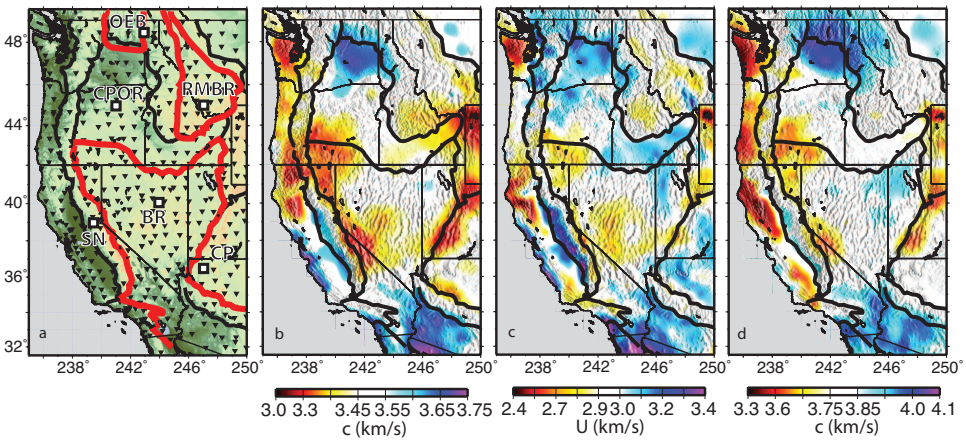

Figure 1: (a) Western US study region. Seismic stations (black triangles), major tectonic boundaries (thick black lines) and boundaries of the predominant extensional provinces (Basin and Range (BR), Rocky Mountain Basin and Range (RMBR) and Omineca extended belt (OEB)) (red lines) are identified. Grid points from the BR, Columbia Plateau Oregon (CPOR), Colorado Plateau (CP), OEB, RMBR and Sierra Nevada (SN) are plotted as white squares. Examples from Figures 2 and 4 correspond to these grid points. (b) Rayleigh wave phase (RP) and (c) group (RG) speed and (d) Love wave phase (LP) speed maps at 20 s period are presented.

6

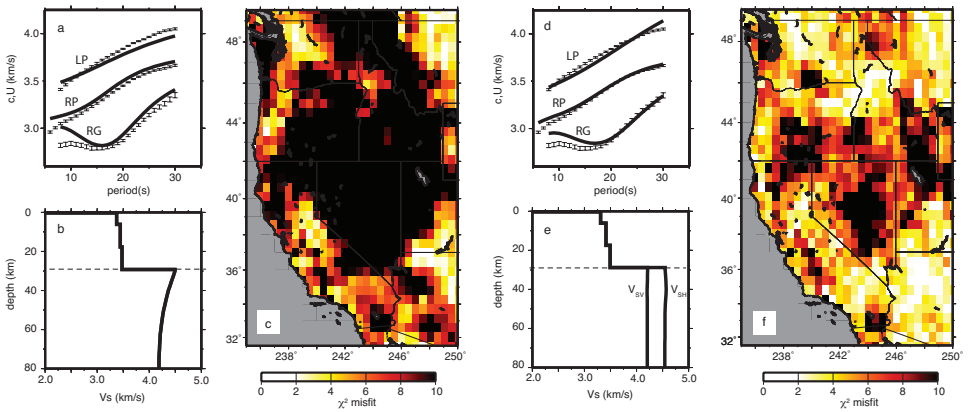

Figure 2: (a) Example local dispersion curves (with 1-σ error bars) compared with black curves predicted by the best-fitting isotropic model, Inversion I, (b) from the BR. Misfit reflects the Rayleigh-Love discrepancy and identifies the need for radial anisotropy. (c) Chi-squared misfit for the best-fitting model from Inversion I; spatially-averaged $\chi^2_I = 12.2$. (d) Same as (a), but fit curves are from Inversion II which includes radial anisotropy in the mantle. (e) Same as (b), but from Inversion II. (f) Same as (c), but from Inversion II; spatially-averaged $\chi^2_{II} = 5.7$. The Rayleigh-Love discrepancy is resolved partially by introducing mantle radial anisotropy.

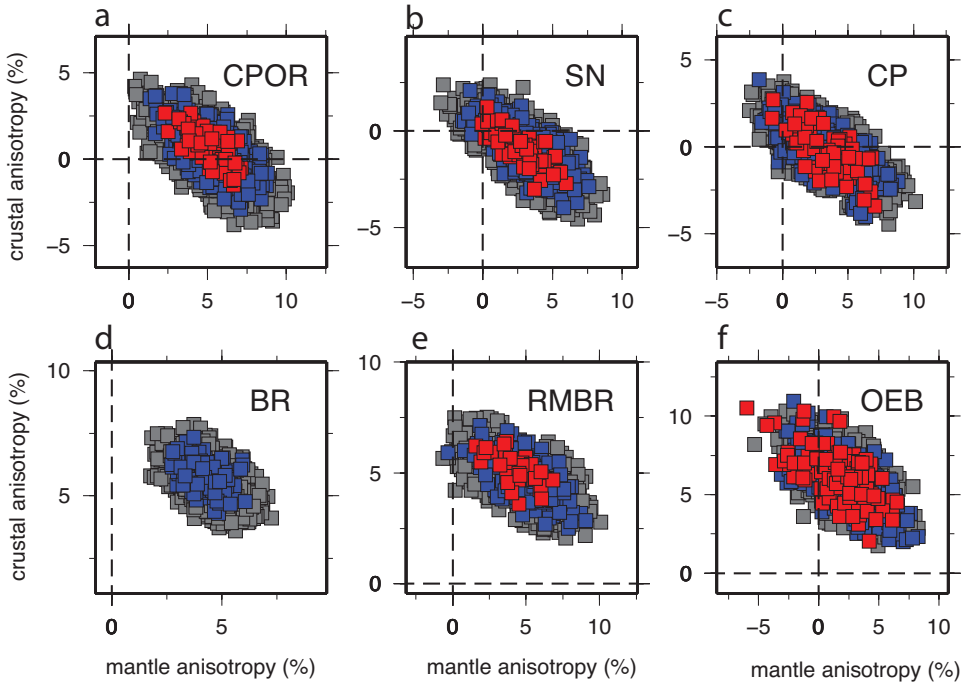

Figure 3: Misfit ellipses reflecting trade-off between amplitudes of crustal and mantle radial anisotropy resulting from inversions with no constraints on the amplitudes of anisotropy in the crust or mantle. Symbol colors correspond to chi-squared misfit: gray denotes $3.0 \leq \chi^2 < 4.0$; blue denotes $2.0 \leq \chi^2 < 3.0$; and red are for $\chi^2 < 2.0$. Results are presented for: (a) CPOR, (b) SN, (c) CP, (d) BR, (e) RMBR, and (f) OEB. The locations BR, RMBR and OEB fall within the principal extensional provinces of the western US.

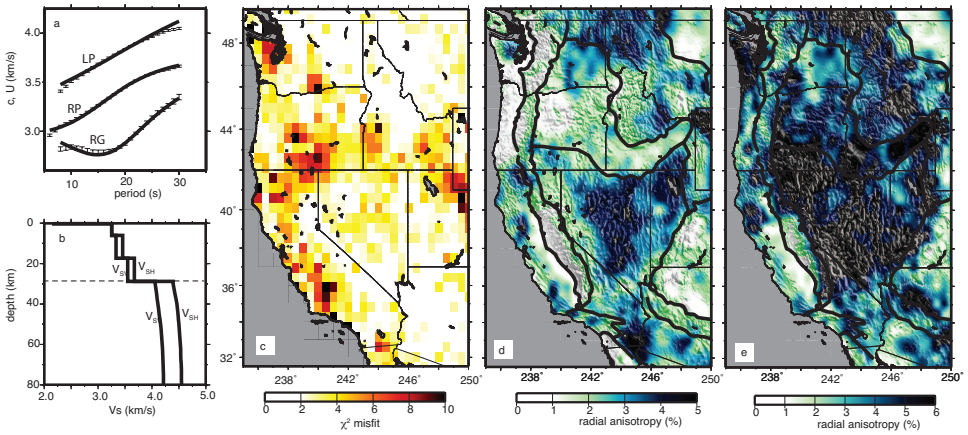

Figure 4: Results from Inversion III, allowing crustal and mantle radial anisotropy. (a) Same as Figures 2a and d, for Inversion III. (b) Same as Figures 2b and e, but from Inversion III. (c) Same as Figures 2c and f, but misfit is for the best-fitting model from Inversion III; spatially-averaged $\chi^2_{III} = 2.8$. The observed Rayleigh-Love discrepancy is largely resolved by introducing crustal radial anisotropy in addition to mantle anisotropy. The amplitudes of radial anisotropy ($2\,|V_{SH} - V_{SV}|\,/(V_{SH}+V_{SV})$) from Inversion III are presented in (d) for the crust and in (e) for the mantle. Extensional province boundaries are drawn with black lines.

7 Methods

Inversion of surface wave dispersion measurements for a 3-D S-wave velocity model proceeds in two steps: (1) the inversion of surface wave dispersion measurements from the inter-station empirical Green's functions by ANT and from earthquake data by MPWT to produce dispersion maps and (2) inversion of the dispersion maps for the 3-D S-wave velocity model. Inversions I, II and III differ only in the amplitudes of radial anisotropy allowed in the deep (middle to lower) crust and in the uppermost mantle.

7.1 Surface wave dispersion maps

Although we make use of two methods to construct surface wave dispersion maps (ANT and MPWT), both techniques yield similar products – maps of surface wave phase and group speeds as a function of period and geographic location. To calculate the dispersion maps by ANT, we have increased the number of stations and, therefore, the areal coverage compared to previously published results[16,17]. In addition, timeseries durations are increased by up to one year. All cross-correlations between 526 stations from the TA were calculated for the time period October 2004 through December 2007 following established methods[15]. Dispersion measurements on the more than 120,000 empirical Green's functions are made by automated frequency-time analysis[31,15] and inverted using straight ray tomography[19]. The resulting Rayleigh and Love wave maps span the period bands, 6 – 40 s and 8 – 32 s, respectively.

MPWT is an extension of the two-plane wave tomography method of Forsyth and Li[32] for larger geographic regions. The Rayleigh wave phase speed maps from MPWT have been updated from published maps[14] to provide dispersion measurements across the western US region. To construct the Rayleigh wave phase speed maps (25 – 100 s period) using MPWT, 250 earthquakes are recorded at the TA between January 2006 and September 2008. Between 25 and 40 s period, where Rayleigh wave phase speeds are estimated by both ANT and MPWT, Yang et al.[14] demonstrate substantial agreement between the phase speed estimates and equivalent resolution in the dispersion maps.

7.2 Data uncertainty estimates

To assess data misfit and select the set of accepted models, uncertainty estimates are required for group and phase speed maps as a function of

position, period, and wave type. Uncertainty estimation for ANT is discussed in detail by Moschetti et al.[23]. Supplementary Figures 2a – d show example uncertainty maps for Rayleigh wave phase speed (RP) at 8, 16, 24, and 40 s period. Uncertainties for RP speeds from MPWT derive from inversion residuals following Yang et al.[14], show little spatial variability, and the spatial average uncertainty is plotted in Supplementary Figure 2e. As described by Moschetti et al.[23] for ANT, Rayleigh wave group (RG) and Love wave phase (LP) speed uncertainties are estimated by a frequency-dependent scaling of the RP speed uncertainty maps of Lin et al.[33]. The scaling parameters derive from the temporal variability of each measurement type as discussed by Bensen et al.[15]. Uncertainty maps for RG and LP speed, therefore, have the same spatial pattern as shown for RP speeds in Supplementary Figures 2a–d. Spatially averaged uncertainties for RP, RG, and LP speed are presented, as a function of period, in Supplementary Figure 2f. The spatial- and frequency-averaged uncertainties in the RP, RG, and LP speed maps from ANT are 14.5, 38.1, and 13.4 m/s, respectively. The spatial- and frequency-averaged uncertainty in the RP speed maps from MPWT is 27.6 km/s.

7.3 Inversions for S-wave velocity

The Rayleigh wave phase and group speed maps and Love wave phase speed maps are inverted simultaneously on a 0.5°-by-0.5° grid across the study region to a depth of 250 km, where the model ties into the S-wave velocity model of Shapiro and Ritzwoller[5]. Inversion parameters include V_P/V_S, V_{SH}, V_{SV} and crustal layer thicknesses, in the crust, and V_{SH} and V_{SV}, in the mantle. Because we find that upper crustal anisotropy cannot resolve the Rayleigh-Love discrepancy, we require the sedimentary and uppermost crystalline crustal layer to be isotropic. Allowed ranges for the inversion parameters are presented in Supplementary Table 1. Crustal thicknesses are constrained by the range provided by receiver function estimates and uncertainties[30]. Details of the inversion are provided in Moschetti et al.[23]. The inversion employs the Neighbourhood Algorithm[21] for parameter space sampling and the radially anisotropic MINEOS[20] code for calculation of surface wave dispersion curves. At least 500,000 trial models, subject to the constraints of Supplementary Table 1, are forward modeled at each grid point. Selection of the final set of models is determined by data misfit, as described below. Inversions I, II and III differ in the amplitudes of radial anisotropy allowed in the deep (middle and lower) crust and in the uppermost mantle. Inversion I is an isotropic model. Inversion II allows

radial anisotropy in the uppermost mantle, and Inversion III allows radial anisotropy in the deep crust and uppermost mantle.

7.4 Model acceptance criteria

At each spatial grid point, and for each of Inversions I, II and III, we accept a set of models that fit the dispersion curves within a specified misfit threshold. We define this threshold as two units greater than the reduced chi-squared misfit, $\chi^2 = n^{-1} \sum_{i=1}^{n} \sigma_i^{-2} (d_i - p_i)^2$ (referred to as "chi-squared"), of the best-fitting model. Here, n is the number of discrete dispersion measurements along the dispersion curves, d_i are the observed local dispersion values, p_i are the predicted dispersion values from a trial model, and σ_i are the measurement errors. At each grid point, we require a minimum of 1000 models to be accepted for the final set of models.

8 References and Notes

31. Levshin, A. L., Pisarenko, V. F., Pogrebinsky, G. A. On a frequency-time analysis of oscillations. *Ann. Geophys.* **28** 211–218 (1972).

32. Forsyth, D., Li, A. in *Seismic Earth: Array Analysis of Broadband Seismograms* (ed.s A. Levander, G. Nolet) 81–97 (AGU Geophys. Monogr., 157, 2005).

33. Lin, F., Ritzwoller, M. H., Snieder, R. Eikonal Tomography: Surface wave tomography by phase-front tracking across a regional broad-band seismic array. *Geophys. J. Int.* **177**, 1,091–1,110 (2009).

(Moschetti, M. P., M. H. Ritzwoller, F.-C. Lin, Y. Yang, Seismic evidence for widespread deep crustal deformation caused by extension in the western US)

Supplementary Information

Inability of additional parameters to resolve the Rayleigh-Love discrepancy

Radial anisotropy is introduced to resolve the Rayleigh-Love misfit discrepancy that exists across large regions of the western US. The question considered here is whether other model parameters can also resolve this discrepancy. The following model perturbations are tested: (1) sediment thickness perturbations outside of the allowed constraints, (2) crustal thickness perturbations, (3) effects of P-wave velocity and P-velocity anisotropy (perturbations to anisotropic parameter ϕ), (4) effects of perturbations to anisotropic parameter η from its isotropic value, (5) mantle anisotropy, (6) crustal anisotropy, and (7) effects of a crustal low velocity zone (LVZ). The results of perturbation tests are presented in Supplementary Figures 5 and 6.

Supplementary Figure 5a presents the fit to the phase speed curves of the best-fitting isotropic model from Inversion I at a grid point in central Nevada (244.0,40.0). The sense of perturbations to the Rayleigh wave group and phase speeds are generally similar, thus group speed fits are not shown. The characteristic misfit is shown in Supplementary Figure 5b. The Rayleigh and Love wave speeds predicted by the isotropic model are fast and slow, respectively, compared to the data. Rayleigh wave misfit is greatest at short periods (<25 s period) and Love wave misfit is largest between about 15 and 30 s period. All results shown here are for the central Nevada grid point.

To determine whether different model parameters can resolve the Rayleigh-Love discrepancy, we perturb various parameters in the best-fitting model from Inversion I. The amplitude, period band, and polarity of the phase speed perturbations (termed a

"sign discrepancy") must match the characteristic misfit of Supplementary Figure 5b to resolve the Rayleigh-Love discrepancy. Modeling the sign discrepancy (e.g., speeding Rayleigh wave speed while slowing Love wave speed) is a critical part of resolving the Rayleigh-Love discrepancy.

Increasing sediment thickness by 2 km yields Supplementary Figure 5c. Rayleigh and Love wave phase speeds both decrease as sediments thicken. Perturbing sediment thickness cannot match the observed sign discrepancy.

The result of increasing crustal thickness by 5 km is presented in Supplementary Figure 5d. Neither positive nor negative crustal thickness perturbations match the observed sign discrepancy in this example. Crustal thickness perturbations are not a viable candidate for resolving the Rayleigh-Love discrepancy as this example illustrates.

In our inversions, we fix anisotropic parameters ϕ and η at their isotropic values. The results of independently perturbing these parameters by 5% are shown in Supplementary Figures 5e and f. These perturbations primarily affect Rayleigh wave speeds, but do so only at periods above about 20 s and at amplitudes that are too small to resolve the Rayleigh-Love discrepancy across the entire frequency band of its observation.

The introduction of +5% ($V_{SH} > V_{SV}$) radial anisotropy in the mantle yields supplementary Figure 5g. Although mantle anisotropy does generate the correct sign discrepancy, it does so only above about 15 s period. Thus, over much of the western US, and particularly over the anisotropic crustal regions, mantle anisotropy alone cannot resolve the observed Rayleigh-Love discrepancy because the mantle anisotropy does not affect surface wave speeds at the shortest periods used in this study.

Similarly introducing 5% radial anisotropy to the middle and lower crust generates Supplementary Figure 5h, which shows the requisite sign discrepancy and comparable amplitudes across the entire frequency band of observation.

Our model parameterizations require that the crustal velocities increase

monotonically with depth. To examine the effect of a crustal low velocity zone (LVZ) on the Rayleigh-Love discrepancy and the strength of radial anisotropy in the crust, we re-invert by allowing a crustal LVZ in the middle or lower crust. We find that for most areas data misfit is not improved by allowing a crustal LVZ, and the best-fitting model typically has crustal velocities that increase monotonically with depth irrespective of whether radial anisotropy is included in the crust. A crustal LVZ does not improve data misfit within the anisotropic crustal regions.

A trade-off between P-wave velocity in the crust and the strength of mantle radial anisotropy has been documented previously[5], and it has been argued that the crustal V_P/V_S values required to resolve the mantle Rayleigh-Love misfit discrepancy are implausibly low. A similar trade-off exists between the strength of radial anisotropy in the crust and the values of V_P/V_S in the crust. To achieve data misfits similar to those observed in this inversion, but in the absence of radial anisotropy in the crust, crustal V_P/V_S ratios must be greatly depressed. Results of an example inversion are shown in Supplementary Figure 6a, which shows the model from Inversion III, and Supplementary Figure 6b, which presents the velocity model that results from an inversion where radial anisotropy is allowed only in the mantle but the crustal V_P/V_S values are allowed to vary between 1.5 and 2.0. The best-fitting model from this inversion has crustal V_P/V_S values that range between 1.56 and 1.58. These values are significantly lower than the estimates of V_P/V_S from body wave studies in this region and elsewhere in the US[34–36] and inconsistent with measurements on rocks from the deep crust[38]. We argue that such low crustal P-wave speeds are physically unrealistic and constrain V_P/V_S to be larger than 1.7 in our inversions (Supplementary Table 1).

To resolve the Rayleigh-Love discrepancy observed for the isotropic model in Supplementary Figures 5a and b, model parameter perturbations must decrease Rayleigh wave speeds, primarily at shorter periods and increase the Love wave speeds at intermediate and longer periods. This requires that model perturbations produce a sign

discrepancy in the perturbations to the surface wave speeds and that the amplitudes of the surface wave speed perturbations be similar to those observed in Supplementary Figure 5b. Of the perturbations tested, physically reasonable mantle and crustal radial anisotropy produce the observed misfit sign discrepancy with perturbation amplitudes sufficient to resolve the Rayleigh-Love discrepancy at periods above 20 s. However, only crustal anisotropy affects the shorter periods that are poorly fit by the isotropic model. The most viable candidate to replace crustal radial anisotropy to resolve the crustal Rayleigh-Love discrepancy is to depress V_P/V_S to values below 1.6. Such values are physically unrealistic for all continental crustal materials, in the deep crust, across the regions of high crustal anisotropy. As summarized in Supplementary Table 1, perturbations to all of the model parameters considered here are included in the Monte-Carlo inversion, but their inclusion contributes primarily to increased model uncertainty.

Supplementary Table 1. Allowed model parameter ranges

Model Parameter	Range	Reference (where applicable)
Sediment thickness	± 250 m	Laske and Masters[39]
Crustal thickness	± 5 km	Gilbert and Fouch[30]
Crystalline crustal layer thickness ratio	1:2:2	
V_S, sediments	1.5 – 3.0 km/s	Christensen and Mooney[37], Brocher[38]
V_S, upper crust	2.0 – 3.5 km/s	Christensen and Mooney[37], Brocher[38]
V_S, middle and lower crust	2.5 – 4.0 km/s	Christensen and Mooney[37], Brocher[38]
V_S, uppermost mantle	3.7 – 4.75 km/s	Shapiro and Ritzwoller[5]
V_P/V_S, sediments	1.75 – 2.5 km/s	Brocher[38]
V_P/V_S, crystalline crust	1.7 – 1.8 km/s	Frassetto et al[36], Brocher[38]
V_P/V_S uppermost mantle	1.8 km/s	Brocher[38]
Crustal density scaling relationship		Brocher[38]
Anisotropy, sediments and upper crust	0%	
Anisotropy, middle and lower crust	Unconstrained	
Anisotropy, uppermost mantle	$\leq$ 10%	Nettles and Dziewonski[22]

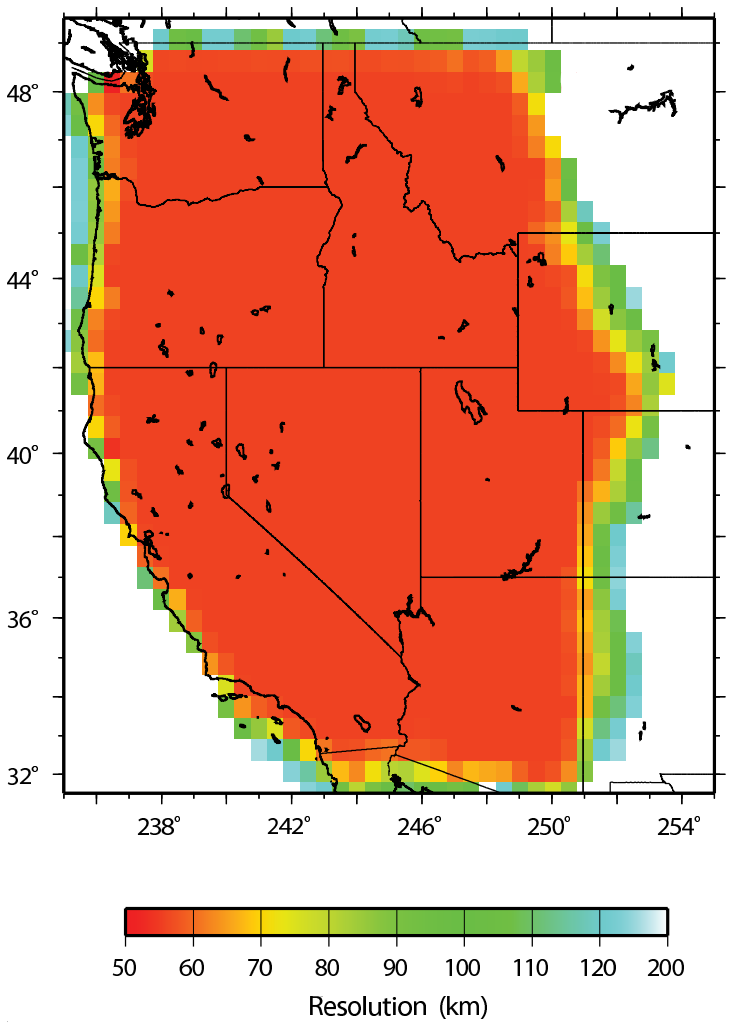

Supplementary Figure 1. Resolution map for the 16 s period Rayleigh wave group speed. Resolution is presented as twice the standard deviation of the Gaussian fit to the resolution surface at each point, as defined by Barmin et al.[19]. Resolution is better than the average inter-station spacing of 70 km within the footprint of the USArray Transportable Array but decays quickly near the periphery of the array.

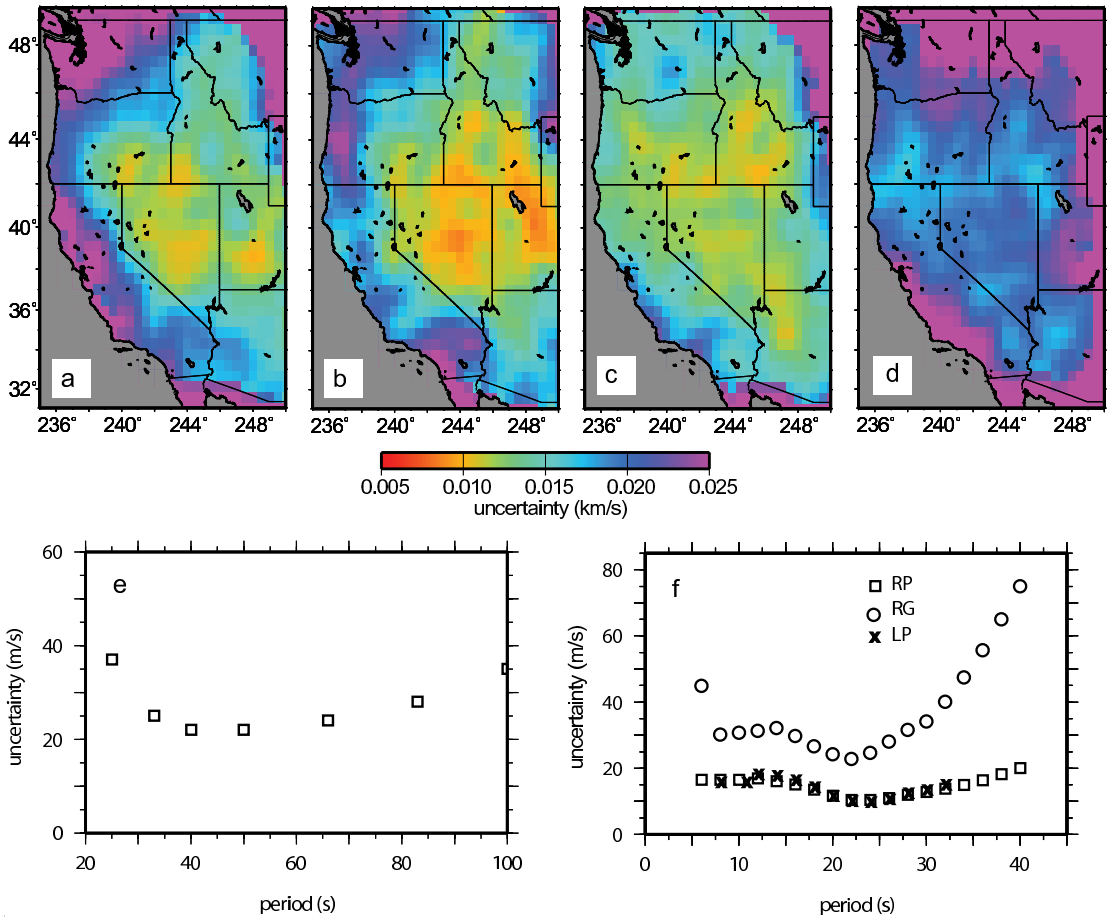

Supplementary Figure 2. Uncertainties in the surface wave dispersion maps. The uncertainties in the Rayleigh wave phase speed maps from Eikonal tomography[33] at 8, 16, 24, and 40 s period are plotted in (a) – (d), respectively. (e) Spatially-averaged uncertainties in the Rayleigh wave phase speed maps from MPWT. (f) Spatially-averaged uncertainties in the Rayleigh wave phase (RP) and group (RG) speed and Love wave phase (RP) speed maps from ANT.

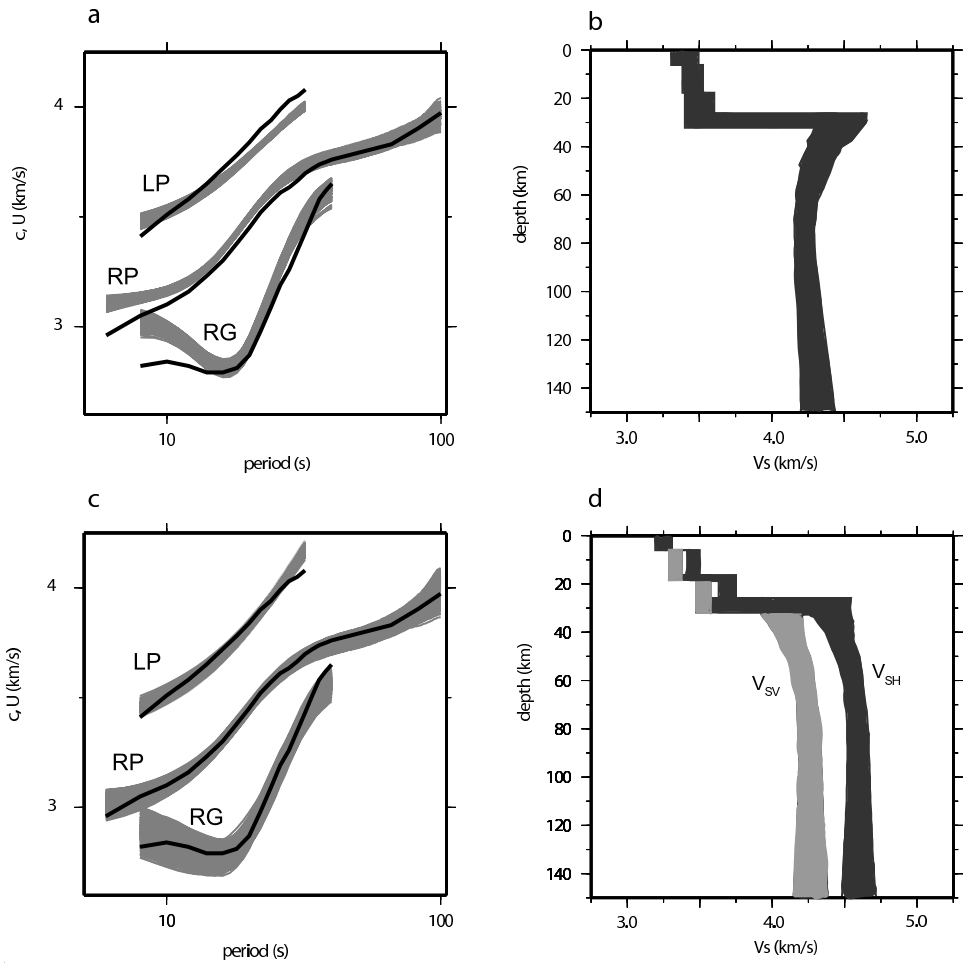

Supplementary Figure 3. The set of acceptable models and corresponding dispersion curves from Inversions I and III at a grid point in central Nevada (244.0,40.0). Inversion I is isotropic in the crust and upper mantle, and its results are plotted in (a) and (b). The results from Inversion III, which permits radial anisotropy in the crust and upper mantle, are plotted in (c) and (d). The Rayleigh wave phase (RP) and group (RG) speed data and Love wave phase (LP) speed data are drawn with black lines, and the dispersion curves for all accepted models are plotted with gray shaded regions in (a) and (c). Accepted models are plotted in (b) and (d) with shades of gray. Chi-squared values for the best-fitting models from Inversions I and III are 29.2 and 3.2, respectively.

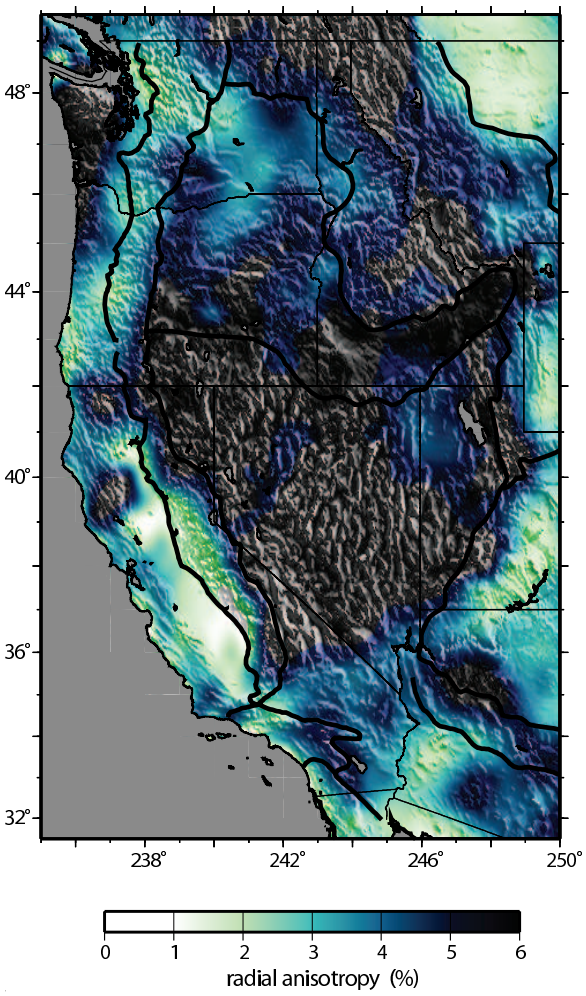

Supplementary Figure 4. Amplitude of radial anisotropy in the mantle from the best-fitting model of Inversion II. Radial anisotropy is not permitted in the crust for Inversion II.

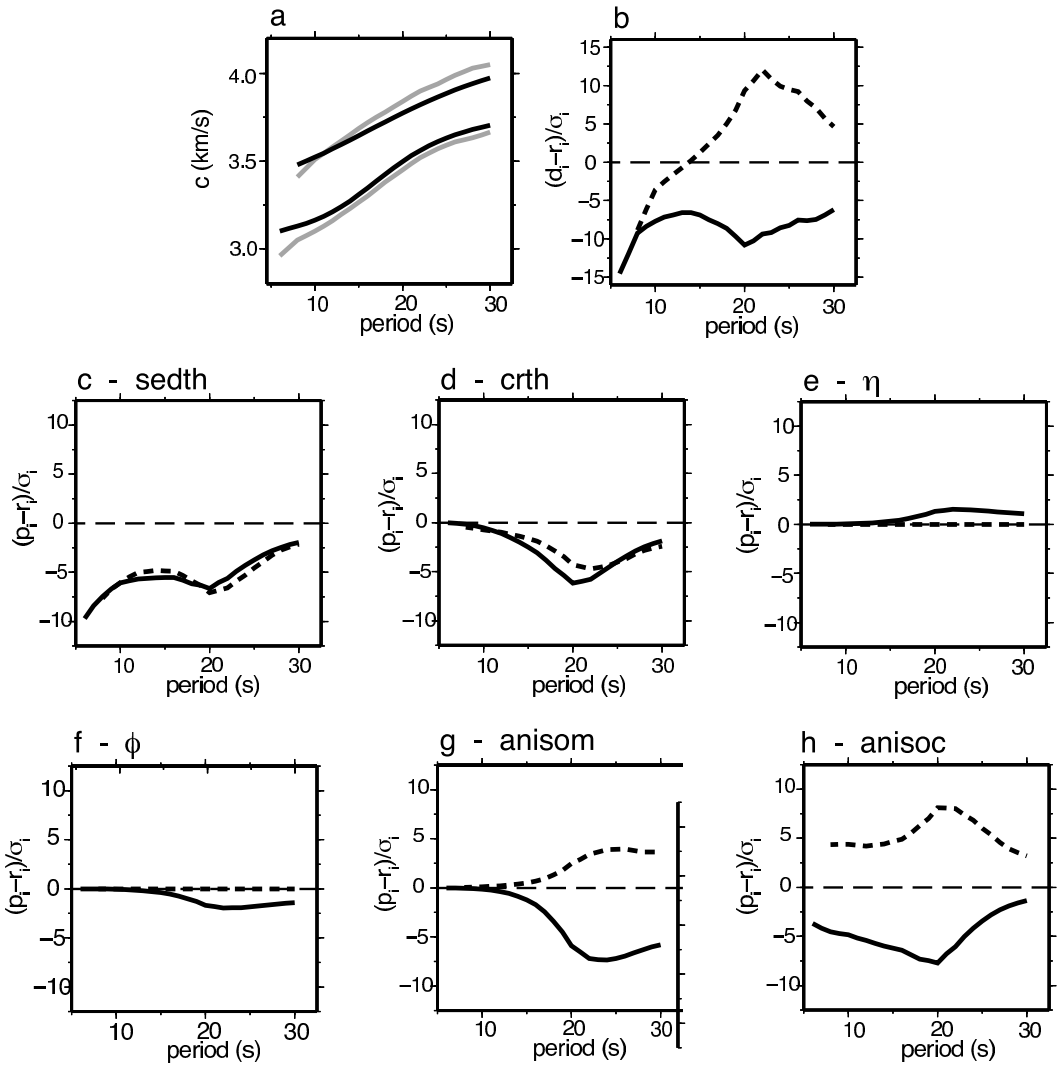

Supplementary Figure 5. Effect of various model parameter perturbations on phase speeds. The Rayleigh and Love wave phase speed data (d_i) from central Nevada grid point (244.0,40.0) and the dispersion curves from the best-fitting model (r_i) of Inversion I are plotted with gray and black lines, respectively, in (a). The misfit of this isotropic model to the Rayleigh and Love wave speeds is plotted with solid and dashed lines, respectively, in (b), and scaled by uncertainty (σ_i). Rayleigh and Love wave phase speeds from the following model parameter perturbations (p_i) are plotted with solid and dashed lines, respectively: (c) sediment thickness, (d) crustal thickness, (e) η, (f) ϕ, (g) mantle radial anisotropy, and (h) crustal radial anisotropy.

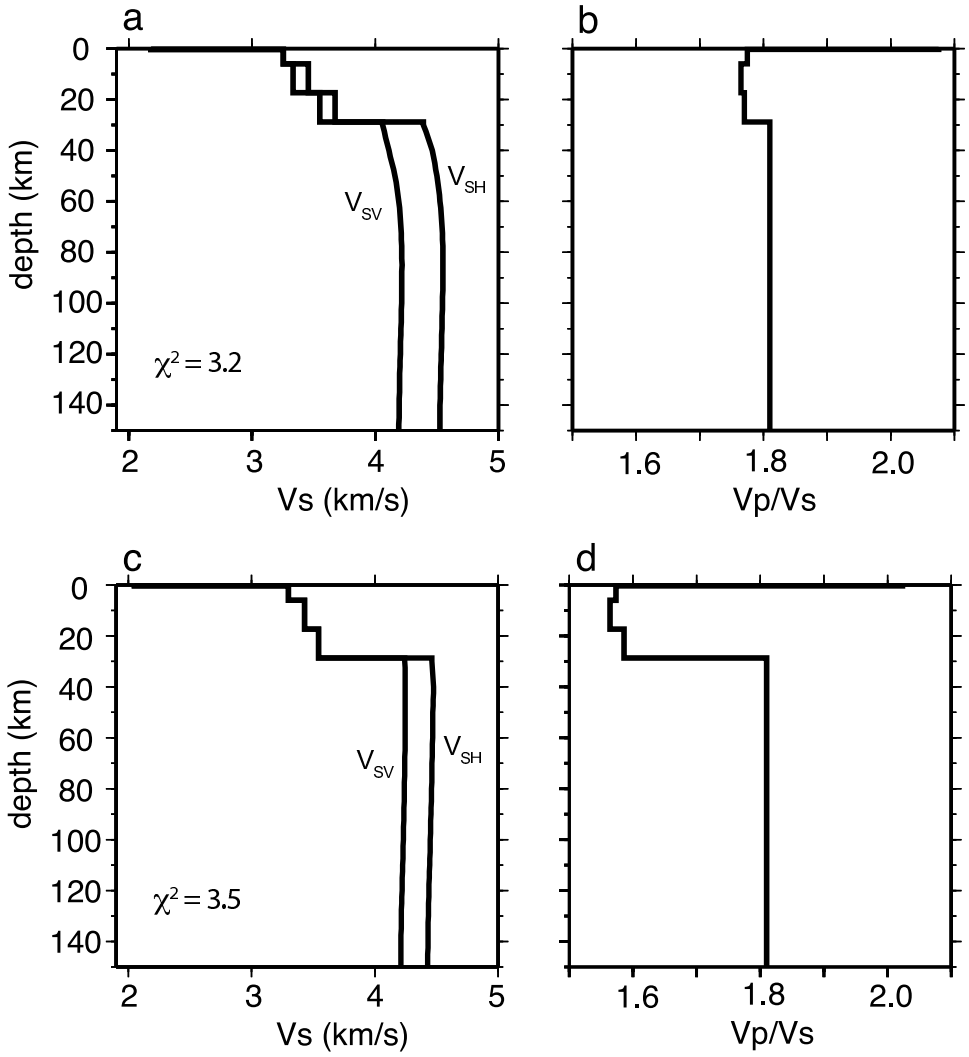

Supplementary Figure 6. Trade-off between the strength of crustal radial anisotropy and V_P/V_S at a central Nevada grid point (244.0,40.0). The best-fitting V_{SH} and V_{SV} models from Inversion III are plotted in (a) where V_P/V_S is constrained to lie between 1.7 and 1.8. The V_P/V_S model at this grid point is plotted in (b). The results from an inversion where radial anisotropy is allowed only in the mantle and the values of V_P/V_S in the crust can vary between 1.5 and 2.0 are plotted in (c) and (d). Chi-squared misfit from the two inversions is similar – 3.2 and 3.5, respectively. However, the V_P/V_S values below 1.6 presented in (d) are physically implausible.

References and Notes

34. Catchings, R.D., Regional $V_P, V_S, V_P/V_S$, and Poisson's ratios across earthquake source zones, from Memphis, Tennessee, to St. Louis, Missouri, *Bull. Seis. Soc. Am.* **89**, 6, 1,591–1,605 (1999).

35. Gilbert, H. J., Sheehan, A. F. Images of crustal variations in the intermountain west. *J. Geophys. Res.* **109**, B03306 (2004).

36. Frassetto, A., H. Gilbert, G. Zandt, S. Beck, and M.J. Fouch, Support of high elevation in the southern Basin and Range based on the composition and architecture of the crust in the Basin and Range and Colorado Plateau, *Earth Planet. Sci. Lett.* **249**, 62–73 (2006).

37. Christensen, N. I. Mooney, W. D. Seismic velocity structure and composition of the continental crust: A global view. *J. Geophys. Res.* **100**, 9,761–9,788 (1995).

38. Brocher, T.M., Empirical relations between elastic wavespeeds and density in the Earth's crust. *Bull. Seism. Soc. Amer.* **95**, 2,081–2,092 (2005).

39. Laske, G., Masters., G. A global digital map of sediment thickness. *EOS Trans. AGU* **78**, F483 (1997).